Effect of a cement-bentonite grout on AVM glass alteration and C-steel corrosion at nanometer scale

Charly Carriere, Alexis Delanoë, Stéphane Gin, Emmanuel Gardes, Isabelle Monnet, Delphine Neff, Eddy Foy, Christelle Martin, Florent Tocino, Nicolas Michau, et al.

Effect of a cement-bentonite grout on AVM glass alteration and C-steel corrosion at nanometer scale

C. CARRIERE[1,*], A. DELANOË[1], S. GIN[2], E. GARDES[3,4], I. MONNET[3], D. NEFF[1], E. FOY[1], C. MARTIN[5], F. TOCINO[6], N. MICHAU[5], J.J. DYNES[7], P. DILLMANN[1]

1 LAPA- NIMBE, IRAMAT, Université Paris-Saclay, CEA, CNRS, 91191 Gif-sur-Yvette Cedex, France

2 CEA, DES, ISEC, DPME, University of Montpellier, Marcoule, F-30207 Bagnols sur Cèze, France

3 Centre de Recherche sur les Matériaux, les Ions et la Photonique (CIMAP), Université de Caen, CEA-CNRS, ENSICAEN, BP 5133, Bd Henri Becquerel, F-14070 Caen cedex 5, France

4 Université Clermont Auvergne, CNRS, IRD, OPGC, Laboratoire Magmas et Volcans, F-63000 Clermont-Ferrand, France

5 Andra, Scientific & Technical Division, 1/7 rue Jean Monnet, 92298 Châtenay-Malabry, France

6 EDF – R&D, Département MMC, site des Renardières, 77818 Moret-sur-Loing

7 Canadian Light Source, 44 Innovation Blvd., Saskatoon, SK, S7N 2V3, Canada

* corresponding author: charly.carriere@ijclab.in2p3.fr

Abstract (300 words max)

Two experimental mockups were operated for one year at 70°C to study the corrosion of C-steel and alteration of AVM glass surrounded by Cox claystone. Only one system included cement-bentonite grout (CBG). Nanometer-scale analyses (TEM, XANES) examined the glass/C-steel interface to assess CBG's effects. The most notable difference was the presence of a nanometric magnetite layer on the C-steel surface in the CBG system. This layer, promoted by the slightly alkaline pH (8–10) solution influenced by CBG, could act as a passivating barrier, potentially mitigating corrosion, although corrosion rates showed no significant differences over one year. A 5 µm-thick sodium-depleted gel layer of disordered SiO_2 formed on AVM glass in both systems, with similar porosity (14–20 nm). The open porosity may limit the gel's protective capacity. However, glass alteration rates decreased over time due to passivation mechanism primarily driven by reduced diffusion through the gel layer, with chemical affinity playing a lesser role. Secondary phases (Si-Fe-O, Si-Mg-O) were detected only in the CBG system, likely originating from the claystone or CBG rather than the glass itself. These findings indicate that CBG had little effect on AVM glass alteration but may enhance long-term C-steel corrosion resistance through magnetite layer formation.

1) Introduction

The French national radioactive waste management agency (Andra) is responsible for the Cigeo project, which investigates the disposal of vitrified high-level radioactive waste (HLW) arising from spent nuclear fuel in deep geological repository. Disposal facility relies on a multi-barrier system including the following materials: glass, steel overpack and casing, cement-bentonite grout (CBG) and claystone. The repository would be located at 500 m below ground in the northeast of the Parisian basin, in the low permeability Callovo-Oxfordian claystone (Cox) [1]. In the studied design, waste packages (borosilicate HLW glass, stainless steel canister and carbon steel overpack) are inserted into cylindrical horizontal disposal cells dug in the Cox, inside a carbon steel (C-steel) casing. The free space between the latter and the claystone is filled with alkaline CBG (pH = 10-11 at 25°C) to neutralize a potential acid transient [2]. Indeed, oxidation of the sulphides in the clays during excavation of the cell generates sulphuric acid. This acid is neutralized by the carbonates in the clay, which generates CO_2 that diffuses into the cell. In turn, the CO_2 can dissolve and lead to acidification of the water in the cell [3], [4].

The multi-barrier system is expected to delay the arrival of groundwater on the radioactive waste package. When groundwater reaches the waste package, corrosion processes starts, releasing Fe into the groundwater. Therefore, glass is altered with a Fe-containing solution. Metal corrosion and glass alteration are expected to occur under anoxia, assuming O_2 consumption. Assessing glass interaction with the materials of the disposal cell (claystone, steel, CBG, groundwater) is crucial to predict the source term, i.e. the flux of radionuclides released by the vitrified waste over time.

The leaching of borosilicate glass by water has been widely studied [5]–[11]. According to interdiffusion and hydrolysis mechanisms, water can exchange protons with alkali elements of the glass (i.e. Na, Li, Cs) acting as modifier and depolymerize the glass network by breaking covalent bonds (Si–O–X, X= Si, Al, Zr, B). These two mechanisms, whether or not they occur at the same time, lead to a hydrated/hydrolyzed interface between the glass and the solution. The glass alteration layer (GAL) is therefore depleted of the elements making of the glass matrix, which end up in solution. Hence the GAL is assimilated to an amorphous layer named “gel”, mostly made of $SiO_{2(am)}$. Their mechanisms of formation are still debated. Depending both on the glass composition and the alteration conditions (e.g. pH, temperature, solution composition) either a dissolution/reprecipitation of aqueous species released at the interface, or a hydrolysis/in situ condensation of partly hydrolyzed Si species play a part in GAL formation [12]–[16]. The self-reorganization of such a gel leads to its densification, becoming a diffusion barrier which can limit the exchange of dissolved species at the interface [13], [17], [18]. Whatever the mechanism at play, the alteration rate can drop down by several orders of magnitude with respect to the initial glass dissolution rate (r_0), according to both the chemical affinity and the passivating effect of the gel [19]. The first driver deals with thermodynamic consideration with the activity of H_4SiO_4 in solution released by glass hydrolysis. The passivating effect is linked to the transport of aqueous species through the passive layer [8].

In actual geological repository conditions, groundwater would contain reactive elements such as Mg, Fe, Ca which could impact glass alteration. Depending on the elements, their concentration, the glass composition and the alteration conditions, some elements can be retained or incorporated in the GAL with a beneficial or detrimental effect on the glass durability [20]–[24]. Besides, glass/iron/claystone interactions experiments (50°C or 90°C, SON68 glass, iron source, Cox groundwater solution, alteration duration) yield Fe and/or Mg phyllosilicates formation within the GAL through a dissolution/reprecipitation mechanism [25]–[32]. Their formation takes out the silica released into the solution, preventing saturation with respect to a passivating gel. Therefore, glass alteration rates remain high, generally close to the initial dissolution rate.

Most experiments involving iron have utilized SON68 glass, which serves as the French R7T7 non-radioactive glass surrogate. Few studies, employing alternative glasses such as ISG glass [21], [33], [34] or PNL 76-68 [35], have reported the formation of iron phyllosilicates. To our knowledge, there is limited information regarding the interactions between AVM glass and iron interactions, except for one of our study and a recent paper [36], [37]. However, AVM glass was developed in Marcoule vitrification facility for high-level wastes arising from gas-graphite reactors [20], [38], and its durability warrants investigation, particularly concerning the influence of CBG on its chemical reactivity.

Our previous work investigated the alteration of the AVM V4 glass (the representative AVM glass [39]) in the presence of CBG and C-steel (70°C, 1 year, groundwater solution). The schematic view of the experiment and the main results are summarized in Figure 1. No significant impact of CBG on glass alteration or steel corrosion was identified after one-year of reaction. Glass dissolution rates were estimated to be 3.4 $\times$ 10^{-2} g.m^{-2}.d^{-1} and corresponded to $r_0^{Cox,\ 70°C}$ / 32 for both systems (assuming isovolumetric alteration [40]), where $r_0^{Cox,\ 70°C}$ is the initial dissolution rate of AVM V4 at 70°C. The C-steel corrosion rates were about 2 µm.year^{-1} and the main iron corrosion products (ICP) were iron carbonates (siderite – $FeCO_3$ and chukanovite - $Fe_2(OH)_2CO_3$ for the system without and with CBG, respectively). Nevertheless, in the presence of CBG, Mg/Fe-rich silicates were observed on the glass surface, while such silicate minerals were not detected in the CBG-free experiment. Interestingly, despite the corrosion of C-steel, no iron enrichment was detected in the GAL. This result significantly contrasts with experiments documented in the literature under similar conditions, where iron phyllosilicates were observed in GAL glass. (mainly for SON68 or ISG glasses) [21], [27], [29], [30], [33], [41]. These initial findings question about the potential passivation capabilities of the observed gel on the glass, both with and without the presence of CBG, that needs more investigation at lower scale. Furthermore, anoxic iron corrosion is a crucial parameter controlling the release of Fe into the solution, and thus glass alteration. This release of iron could be linked to the presence, or not, of an iron oxide less porous interfacial layer (IL) at the metal/ICP interface, controlling the corrosion rate by playing a diffusing barrier [42]–[44], [68]. This oxide layer was found by several studies on low alloy steel in carbonated and clayey environments [45]–[49].

To address these inquiries, the present study provides supplementary nanometric-scale characterizations using TEM and STXM within the system above described [36]. Analyses focus on the gel and at the C-steel/ICP interface to investigate the potential formation of interfacial layers. Nanostructural characterizations of the AVM V4 GAL reveal the formation of a gel and its porosity contributing to a deeper understanding of the long-term glass alteration behavior [27], [50], [51], particularly under the influence of a CBG-buffered pH. The origin of the Mg/Fe-rich silicates is also examined.

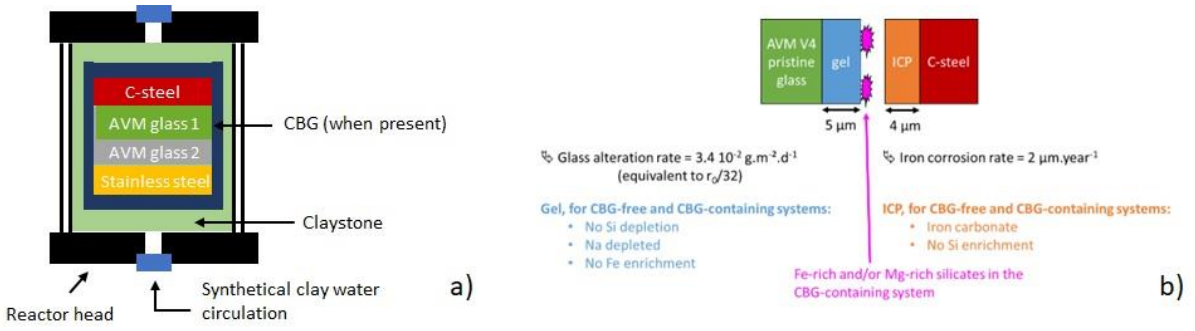

Figure 1: Schematic view of the experiment (a) and synthetic representation of published results observed at AVM glass/C-steel interface (a) [36]. (ICP: Iron corrosion products, r_0: initial AVM V4 glass dissolution rate at 70°C).

2) Materials and methods

2-1) AVM glass/steel/claystone systems with and without cement-bentonite grout

The studied systems are composed of a stack of 309 stainless steel/AVM glass 1/AVM glass 2/P285NH C-steel, surrounded by Callovo-Oxfordian claystone, located inside a reactor [36]. Two experimental setups were prepared and subjected to identical conditions (70°C, 1 year, anoxia): (1) a mockup experiment without CBG and (2) a mockup experiment containing CBG, a low pH cementitious grout. In the CBG-containing system, this filler material was introduced between the stack of materials and the Cox claystone (with a CBG/Cox mass ratio close to 1/100). CBG is composed of Cement CEM III/C, silica fume, bentonite, hydrotalcite and water [52]. Compositions of AVM glass, P285NH C-steel and CBG are given in Table 1,

Table *2* and Table 3, respectively. The stacks of materials were saturated with synthetic Cox groundwater (Table 4), and placed in an oven at 70°C for 1 year, in anoxic conditions. The Cox claystone was provided by Andra's underground research laboratory located in Bure (France). The synthetic Cox groundwater is a solution in equilibrium with Cox claystone, at 70°C (pH = 6.86, Eh = -0.14 V/SHE) [53]. This solution was prepared by dissolution of salts ($NaHCO_3$, Na_2SO_4, Na_2O_3Si, NaCl, KCl, $CaCl_2$, $MgCl_2$, $SrCl_2$) and the pH was adjusted with CO_2 bubbling. Water circulation occurred from bottom to top. Full details of the experimental setup have already been published [36], as an initial study was conducted on these mockup experiments.

Table 1 : Composition of AVM V4 glass (wt.%).

Oxides	SiO_2	B_2O_3	Na_2O	Al_2O_3	MgO	Fe_2O_3	F	others
Content	43.37	17.43	17.28	10.92	4.32	0.90	0.72	rest

Table 2 : Composition of the steel P285NH (wt.%).

Element	C	Si	Mn	Ni	Cr	Cu	others	Fe
EN 10222-4	0.18	0.4	0.6-1.5	0.3 max	0.3 max	0.2 max	0.29 max	rest

At the end, the mockups were dismantled, and the stacks of materials were embedded in a bicomponent resin without freeze-drying, and cut into cross section. No precautions were taken during the changeover from anoxia to air, without changing the phases formed, in particular corrosion products [36]. Cross sections were polished with ethanol, using SiC papers (500, 800, 1200, 2400, 4000) up to 5 µm, followed by diamond suspension polishing at 3 µm and 1 µm. The cross sections were cleaned in acetone and ethanol (3 min duration each) with ultrasound. Samples were stored under vacuum to prevent oxidation.

Table 3 : Constituents of the CBG.

Components	quantity (kg/m^3)
Cement CEM III/C 32,5 N SR CE PM NF	126
Silica fume	126
Bentonite	33.6
Hydrotalcite	8.4
Water	881

Table 4 : Chemical composition of the synthetic Cox groundwater.

	Na	K	Ca	Mg	Sr	Si	Cl	SO_4	HCO_3	Eh V vs. SHE	pH
mg/L	966	39.1	397	99.6	17.5	9.8	1453	1345	232	-0.14 V	6.86

2-3) Analytical techniques

Four thin foils of the cross sections were extracted from the GAL and ICP using FEI Helios Nanolab 660 scanning electron microscope/focused Ga^+ ion beam (SEM-FIB). A 1 µm thick Pt layer was deposited on the surface of interest (i.e. glass alteration layers, silicates, ICP), to protect it from Ga^+ ions beam. Thin foils were cut and extracted from the matrix using a Ga+ ion beam and thinned to 1 µm or 100 nm thickness, depending on the envisaged analyses (see after) at 0.43 nA, 0.23 nA and 80 pA ion current. Finally, in order to reduce irradiation defects induced by the 30 keV Ga^+ ion beam [54]–[56], the thins foils were cleaned on both faces with a low intensity and low energy beam: 28 pA at 5 kV, then 72 pA at 2 kV, and 72 pA at 1 kV for a few minutes.

High-resolution transmission electron microscopy (HRTEM) was performed at 200 kV on a JEOL F2010 F electron gun, equipped with a diode EDAX X-ray microanalysis for electron diffraction. The analyses were performed on 100 nm-thick foils, and the micrographs were acquired using *Digital Micrograph* software from Gatan. The d_{001}-spacing of silicate sheets and the gel porosity were measured from the HRTEM images with *ImageJ* software.

FIB foils were characterized at the Si K- and the Fe L-edges using the Scanning Transmission X-ray Microscopy (STXM) on the SM beamline at the Canadian Light Source (CLS) synchrotron [57], and on the HERMES beamline at the Soleil synchrotron[58], respectively. This technique provides nanometer scale investigations around the absorbent atom, with a 30 nm spatial resolution and 0.1 eV energy resolution. Image sequences (i.e., stacks) at the Fe L-edge were collected on 100 nm thick thin foils inside iron silicates observed by the TEM analysis, provide iron valence [45], [59], [60]. To probe the silicon chemical environment up to 0.5 or 0.6 nm distance [61]–[63], stacks were collected on 1 µm-thick thin foils using the Si K-edge. The as-collected transmission 2D-images on the thin foils were converted to absorption 2D-images using the incidence flux (I_0) obtained from areas devoid of sample. Thus, for each pixel of a stack, a XANES (X-ray absorption near edge structure) spectrum can be reconstituted. Principal Component Analysis (PCA) – cluster analysis (CA) was performed on each stack to identify clusters of spectra, corresponding to specific areas on the map. All data analysis was performed using *Axis2000* software. The PCA-CA derived spectra were compared with reference spectra published in the literature. The Si K-edge spectra were modeled with combination of iron phyllosilicates reference and $SiO_{2(am)}$ spectra [26]. The Fe L-edge spectra were modeled by combination of reference spectra of phase presenting a "pure" Fe^{II} and Fe^{III} valence: siderite and maghemite phases respectively.

The potential-pH diagram presented in this paper was plotted with *The Geochemist Workbench 12.0* software and the thermodynamic database "Thermochimie v10a electron" [64], which is available online for free (https://www.thermochimie-tdb.com/). Chukanovite thermodynamic data were implemented in the database as this mineral was not included (log(K)=2.97 according to *thermochimie v11a*). Act2 mode was used to plot the diagram at 70°C. This mode determines the most thermodynamically stable phases, from an input solution and a minerals selection. The theoretical Cox groundwater composition was used as input, and phases of interest were included in the model (iron, Fe-carbonates, maghemite, magnetite, Fe^{2+}, Fe^{3+}, Fe-hydroxides, Fe-sulfates, Fe-chlorides, H_2, HCO_3^-) according to the characterizations and the phases mentioned in the literature. Theoretical Cox groundwater composition does not contain Fe data, so Fe^{2+} input activity was deduced from

Gailhanou's paper [65] and set at 5.7 10^{-5} mol.L^{-1} to allow for iron phyllosilicate formation. The thermodynamic constants of the mineral are presented in Table 5.

Table 5: Phases considered for the potential-pH diagram (data from Thermochimie v10a electron).

Phase	Chemical formula	Equation	log Ks at 70°C
Chukanovite	$Fe_2CO_3(OH)_2$	Chukanovite + 2 H^+ ⇄ 2 Fe^{2+} + 2 H_2O + CO_3^{2-}	2.97
Siderite	$FeCO_3$	Siderite ⇄ Fe^{2+} + CO_3^{2-}	-11.08
Maghemite	γ-Fe_2O_3	Maghemite+ 6 H^+ + 2 e^- ⇄ 2 Fe^{2+} + 3 H_2O	24.96
Magnetite	Fe_3O_4	Magnetite + 8 H^+ + 2 e^- ⇄ 3 Fe^{2+} + 4 H_2O	30.51
Iron	Fe	Fe ⇄ Fe^{2+} + 2 e^-	13.79
Fe^{3+}	Fe^{3+}	Fe^{3+} + e^- ⇄ Fe^{2+}	12.53
$Fe(OH)_2$	$Fe(OH)_2$	$Fe(OH)_2$ + 2 H^+ ⇄ Fe^{2+} + 2 H_2O	17.85
$Fe(OH)^+$	$Fe(OH)^+$	$Fe(OH)^+$ + H^+ ⇄ Fe^{2+} + H_2O	8.23
$FeHCO_3^+$	$FeHCO_3^+$	$FeHCO_3^+ \rightleftarrows Fe^{2+} + CO_3^{2-} + H^+$	-11.77
$Fe(CO3)_3^{3-}$	$Fe(CO3)_3^{3-}$	$Fe(CO)_3^{3-} + e^- \rightleftarrows Fe^{2+} + 3CO_3^{2-}$	-11.71

3) Results and discussion

3-1) Steel corrosion products

Thin foils were taken in the 4 µm-thick corrosion products of the systems, where the Fe^{II} iron carbonates devoid of silicon were already identified (respectively siderite and chukanovite without and with CBG). More specifically, analyses focused at the C-steel/ICP interface using STXM at the Fe L-edge (Figure 2). For both systems, following the procedure indicated in Materials and methods section, two main oxidation states, Fe^0 (yellow) and Fe^{II} (blue) (Figure 2-c and f), were distinguished by PCA in the regions of interest (ROI, materialized by the dotted white squares in Figure 2-a and d). These oxidation states were deduced by comparison with the STXM spectra database at Fe-L edge [45], and referred to uncorroded steel (Fe^0) and iron carbonate (Fe^{II}) respectively, confirming the results obtained at microscopic scale [36]. Furthermore, on the CBG system, an additional interfacial corrosion products layer (IL, in red in the Figure 2-e), ranging between 200 nm to 400 nm and adjacent to the steel, was detected by PCA (see methodological part). The IL extracted spectra corresponding to this zone (Figure 2-f) present a mixed valence inferred from the relative intensity of the L_3-a and L_3-b edges. It corresponds to a predominantly Fe^{III} species, i.e. 33% Fe^{II} and 67% Fe^{III} (Table 6), with good fit parameters (R^2 = 0.99 and χ^2 = 0.4), comparable to the valence state of magnetite (Fe_3O_4). This iron oxide was previously identified at the steel/carbonates interface when C-steel was corroded in carbonated and anoxic environments [45], [46], [48], and was also detected in the presence of the CBG [3], [66], [67]. However, literature concerning an integrated glass/steel/claystone experiment is comparatively limited [30], [32].

Table 6: Decomposition of the interfacial layer spectra collected at Fe L-edge in the steel corrosion products faced to AVM glass with CBG.

Spectra	decomposition (± 2)	R^2	χ^2
Interfacial layer, with CBG (Figure 2-f)	33 % Fe^{II} + 67% Fe^{III}	0.99	0.4

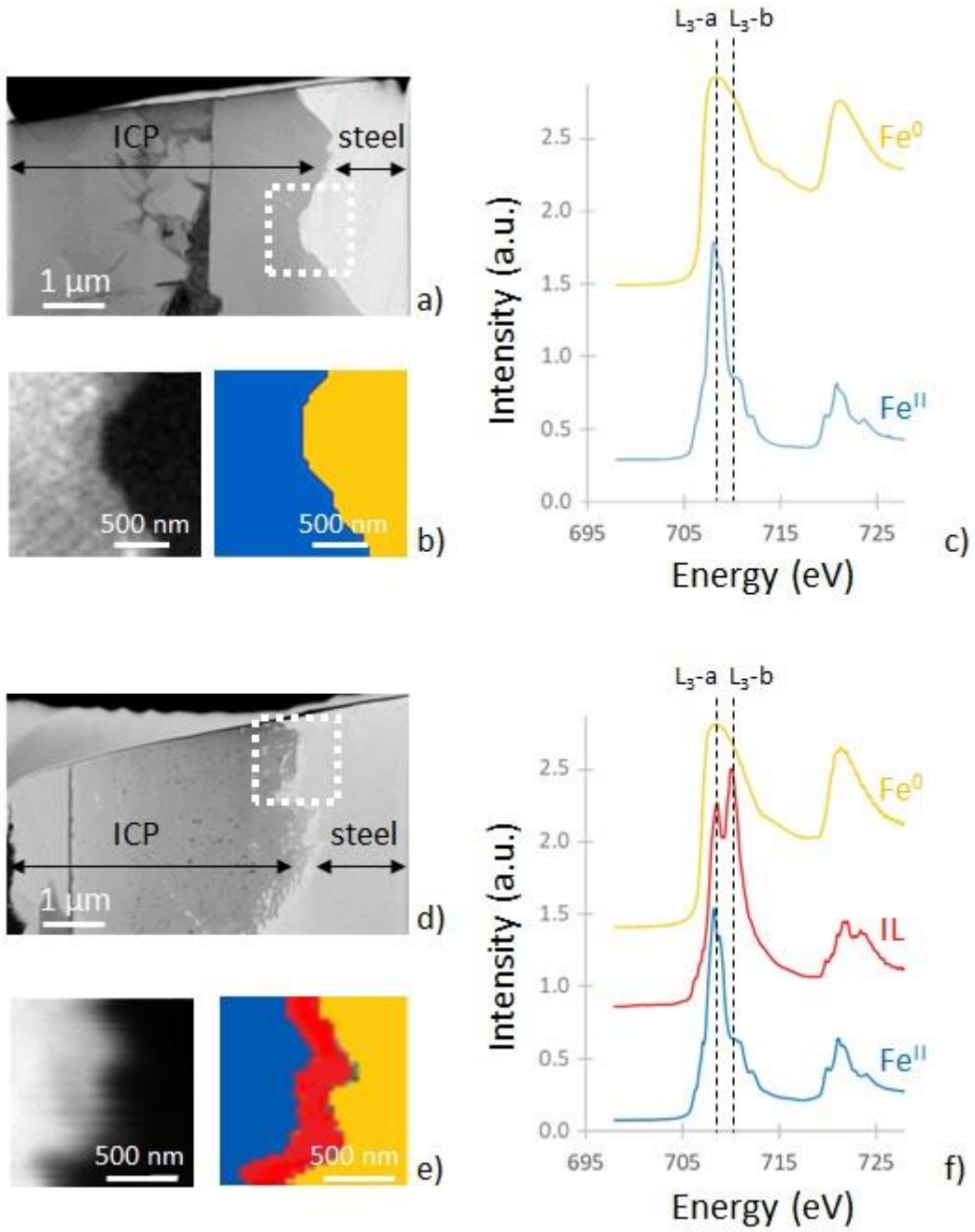

Figure 2: STXM analyses at Fe L-edge performed in the steel corrosion products faced to AVM glass with and without CBG. STEM micrographs of the FIB foils taken in the corrosion layer without (a) and with (d) CBG. The dotted white squares show the region of interest (ROI) including the interfacial layer (IL). The composite color-coded maps, obtained in these ROI at Fe L-edge after statistical treatment without (b) and with (e) CBG, indicate two or three main components: metallic iron Fe^0 in yellow, an interfacial layer (IL) in red and carbonate Fe^{II} in blue. The Fe L-edge colored spectra without (c) and with (f) CBG are associated with the two and three colored ROI.

Thermodynamic diagram of iron in Cox groundwater was calculated using detected and/or expected Fe-phases in such an experiment (Figure 3), with the alteration conditions (70°C, groundwater composition) and reaction equations given in Table 7. Metallic iron is not stable in water and three thermodynamically stable species are suggested according to potential/pH values: maghemite, siderite and magnetite. Note that chukanovite, the metastable hydroxycarbonate with respect to siderite [68], does not appear. At the initial conditions, i.e. Eh = – 0.14 V/SHE and pH = 6.9, siderite should be

favoured. The activity of iron, released through generalized corrosion, can influence the local potential of water according to the Nernst equation (1),

$$E = E°_{Fe^{3+}/Fe^{2+}} + 2.3\frac{RT}{nF} log \frac{a(Fe^{3+})}{a(Fe^{2+})} \quad (1)$$

where E and $E°$ are the potential and standard potential respectively, R the universal gas constant, T the temperature, n number of electrons exchanged, F the Faraday constant and a the activities of aquous species. The latter have been estimated for the pore water in a clay-rock material at the expected p_{CO2} and temperature according to previous works [27], [65]. The calculated iron concentrations of $[Fe^{2+}] = 5.7.10^{-5}$ mol.L^{-1} and $[Fe^{3+}] = 3.5.10^{-19}$ mol.L^{-1} led to a potential E = - 0.2 V/SHE, a value close to the initial potential which can be measured in the claystone. Hence a minimum pH increase, at around 8, is required to promote magnetite formation in our experiment.

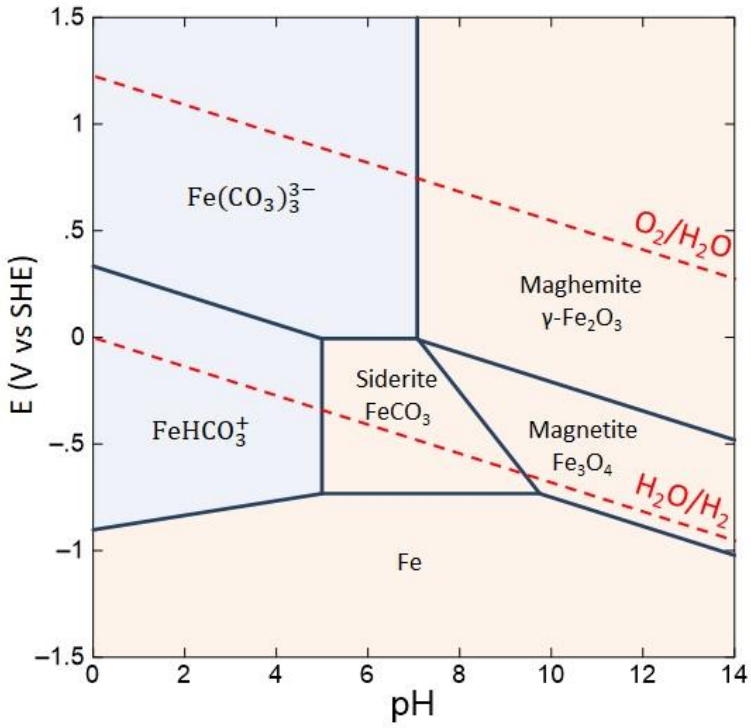

Figure 3: Iron potential-pH diagram in carbonated environment calculated at 70°C with the initial synthetic Cox groundwater composition. Dissolved and solid species are respectively in blue and yellow. Phases and reaction considered are presented in Table 5 and Table 7, respectively.

Table 7 : Reactions and equations of the potential-pH diagram in Figure 3.

Reactions	Line equation
$Fe(CO)_3^{3-}$ + H^+ + e^- ⇄ $FeHCO_3^+$ + 2 CO_3^{2-}	y = 0.334-0.068x
2 $Fe(CO)_3^{3-}$ + 3 H_2O ⇄ Maghemite + 6 CO_3^{2-} + 6 H^+	y = 7.076
$Fe(CO)_3^{3-}$ + e^- ⇄ Siderite + 2 CO_3^{2-}	y = -0.006
$FeHCO_3^+$ ⇄ Siderite + H^+	x = 4.995
Maghemite + 2 CO_3^{2-}+ 6 H^+ + 2 e^- ⇄ 2 Siderite + 3 H_2O	y = 1.439-0.204x
Maghemite + H^+ + e^- ⇄ Magnetite + 5 H_2O	y = 0.472-0.068x
Magnetite + 3 CO_3^{2-}+ 8 H^+ + 2 e^- ⇄ 3 Siderite + 4 H_2O	y = 1.923-0.272x

While the presence of magnetite is not confirmed in the CBG-free system in our study, this mixed oxide phase is unequivocally identified in the presence of CBG. The nanometric interfacial Fe^{III}-rich layer is particularly significant as it may decrease the corrosion rate and potentially passivate the metal, serving as a diffusive barrier. Whether it corresponds to magnetite (Fe_3O_4) or maghemite (γ-Fe_2O_3), this layer plays a crucial role [42], [43], [49], [69], [70]. Although corrosion rates are similar in both systems after one-year of reaction, it could be different for longer alteration times. Hence the contribution of CBG addition appears justified to favor magnetite formation due to its pH buffering capacity in alkaline conditions. Although only a few papers are available in the literature regarding CBG evolution, the pH of a solution containing CBG stabilizes around 10 after several months. [2], [3], [71].

3-2) Glass alteration layers

Facing to C-steel, the alteration layers formed on AVM glass, with and without CBG, were investigated at nanometer scale. As a reminder, after one-year alteration, a 5 µm-thick, Na-free layer containing the same concentration of Si as in the pristine glass (PG) was observed in both systems [36]. This observation was supported by glass alteration markers, i.e. Si/Al and Na/Al ratios with the constant total content of Si + Al + Na = 43 % in PG than in GAL (Table 8) [36]. Although the alteration solution was not recovered and analysed, it is also expected that B contained in the glass must has been dissolved congruently with Na [72].

Table 8: Glass alteration markers determined by SEM-EDS in the pristine glass and in the gels formed on AVM V4 faced to C-steel in both systems (raw data were published in the previous work [36]).

Alteration markers	Pristine glass	Gel, system without CBG	Gel, system with CBG
Si-Al-Na (wt.%)	43	43	43
Si/Al	3.3	3.6	3.4
Na/Al	1.9	0.2	0.3-0.4
Mg/Al	0.4	0.2	0.2

STXM analyses were performed at Si K-edge in the GAL to collect nanostructural data (Figure 4). For both systems (without and with CBG, Figure 4-b and Figure 4-d respectively), Si K-edge spectra show an intense absorption peak at 1846.6 eV (noted A) and a broad peak around 1863 eV (noted D). These two peaks, corresponding to the fourfold coordinated Si atoms and neighboring O [30], [73], respectively, are also observed on the Si K-edge spectrum obtained in the pristine glass (Figure 4-b, grey spectrum). This comparative approach suggests the GAL formed in both systems are made of a disordered network, close to amorphous SiO_2 [26] even though they also contain some other minor elements. This result markedly differs from that obtained on SON68 glass, for which an ordered iron silicate network is frequently observed when the glass is altered in Cox groundwater in the vicinity of an iron source [25]–[27], [29], [41]. In these systems, iron phyllosilicates form by a dissolution/reprecipitation mechanism. As opposed to a micro/nanostructured Fe-rich GAL, the term “gel” will be used instead of “GAL” for the remainder of the article.

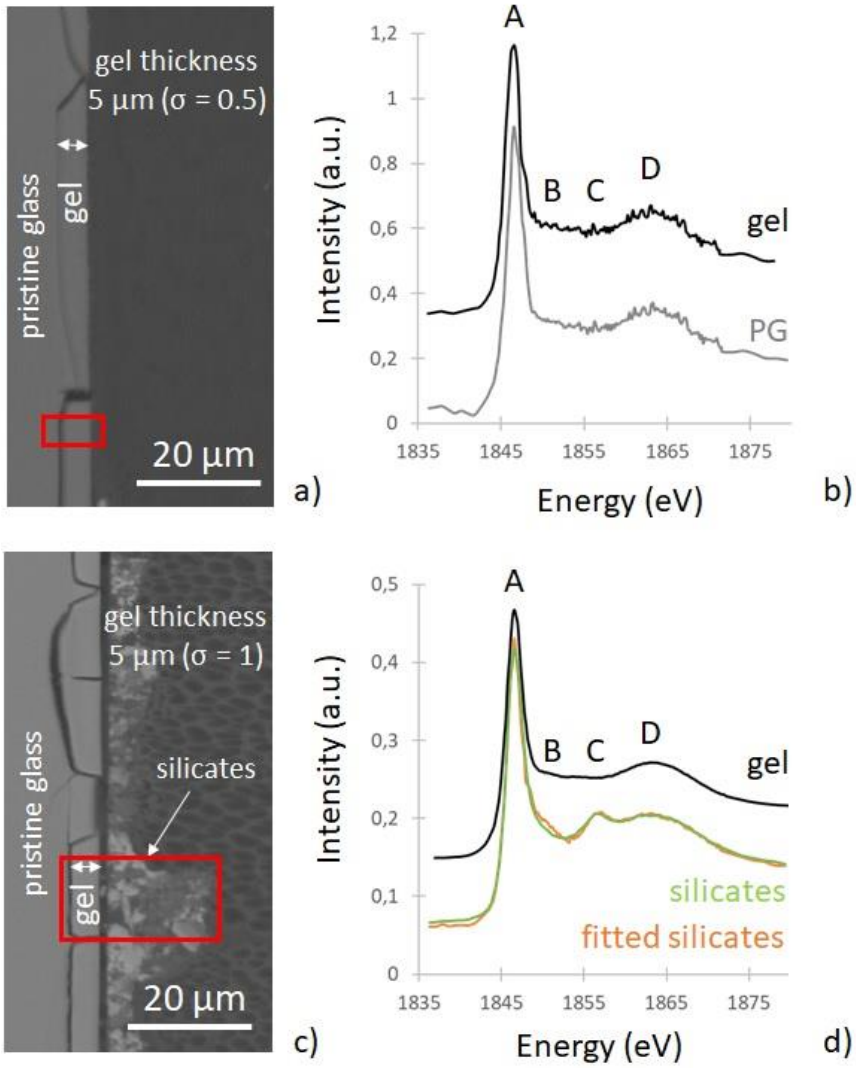

Figure 4: Scanning electron micrographs (backscattered electron) of the AVM glass cross section faced to C-steel in the CBG-free (a) and CBG-containing (c) systems. STXM spectra collected in the region of interest (i.e. pristine glass, gel and silicates when present) for the CBG-free (b) and CBG-containing (d) systems. Cracks in the gels were formed during sample preparation.

Depending on the glass alteration mechanism, a low porosity gel can form and enhances its protective properties, limiting exchange between glass and solution species, and increasing Si retention in the GAL [13], [51], [74], [75]. To better understand the passivation mechanism of AVM glass, the microstructure of the gels was investigated using high resolution transmission electron microscopy (HRTEM). As expected, no visible pores were detected in the pristine glass (Figure 5-a). Note that the resolution of the HRTEM, combining analysis limits and our measurement error, is around 1-2 nm. Conversely, spherical shaped pores were detected in the two gels. According to image processing, about one third of the area is covered by pores. While an overlap of pores located at various depths within the ~100 nm thick foil cannot be excluded, which may lead to a possible bias in the measurement, a reasonable estimation of pore diameters can be provided. According to TEM micrographs in both systems (Figure 5-b,c), pore size is ranging between 14 nm to 20 nm (17 nm average, σ = 2 nm, 20 values). Although the literature reports pore size within gels ranging between <1 nm up to 80 nm depending on the conditions (e.g. glass composition, alteration conditions, …) [14], [15], [39], [40], [50], [76], no data on gel porosity are available regarding specifically AVM glass. However, if one consider valid what has been obtained on other borosilicate glasses such as ISG, a

passivating gel is expected at the nanometer range [14], [72]. This would suggest that the large pores observed in the gel formed on AVM glass should render the gel less protective than a gel with a clogged porosity.

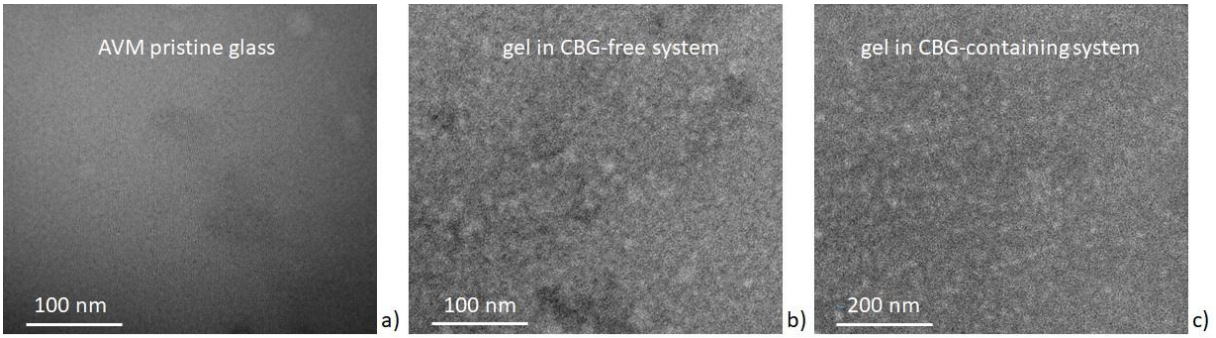

Figure 5: HRTEM analyses of gels formed on AVM glass faced to C-steel in the PG (a), in the gel of the CBG-free system (b) and in the gel of the CBG-containing system (c). Pores apprear in light-grey on these images. No pores are visible in PG. Pores with diameters ranging between 14 nm and 20 nm (17 nm average, σ = 2 nm, 20 values).

The only difference regarding the two systems is the presence of Si-Fe-O and/or Si-Mg-O secondary phases on top of the gel only in presence of CBG. In our previous paper we suggested that these phases had formed during the experiment [36]. Here their formal characterization proves that they were provided by claystone and/or CBG rather from precipitation from glass elements, as no silicon depletion occurred in the glass. HRTEM analyses performed in the Si-rich phases indicate the presence of crystallized clay sheets (Figure 6), with inter-reticular distances of 12.4 Å (σ = 1.5 Å, 45 measurements), corresponding to the d_{001} distance of smectite [77]–[79]. Then STXM spectra at Si K and Fe L-edges were collected for smectite identification at the same location. Si K-edge spectra (Figure 4-d, green spectrum) present two absorption peaks at 1846.6 eV (A) and 1863.3 eV (D), but differ from $SiO_{2(am)}$ with a peak at 1856.8 eV (C).

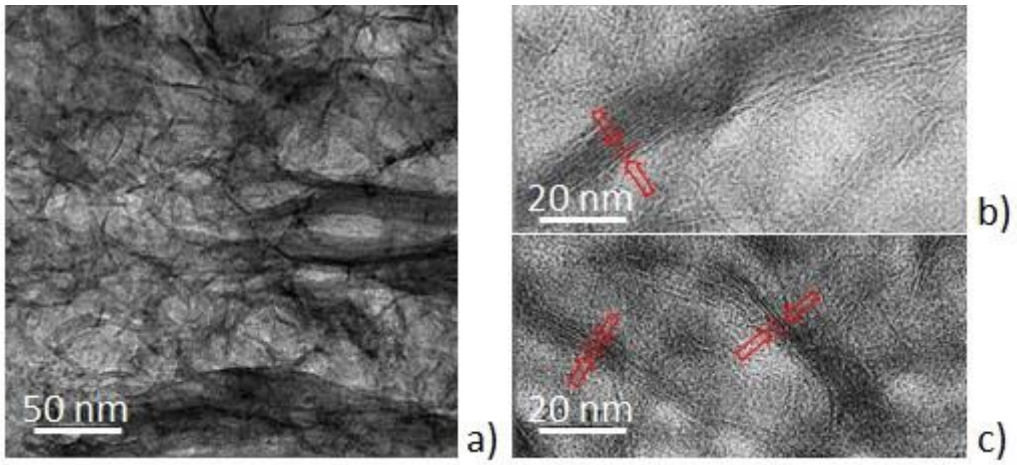

Figure 6: HRTEM analyses performed in the Si-Fe-O and Si-Mg-O phases along the gel surface in the system containing CBG. (a) HRTEM micrographs highlight the presence of crystallized clay sheets. (b) and (c) magnified HRTEM micrographs of the crystalline phases with inter-reticular distance of 12.4 Å (σ = 1.5 Å, 45 measurments) compatible with smectite group.

Then experimental spectra were decomposed by linear regression using the reference database of $SiO_{2(am)}$ and smectites (3 saponites, 2 nontronites, 1 hectorite and 1 montmorillonite [26]). Best fit (Figure 4-d, orange spectrum) was obtained with 57% of montmorillonite, 17% of nontronite and 26% of $SiO_{2(am)}$ (Table 9), identifying 2 dioctahedral smectites (montmorillonite and nontronite) and a Si-amorphous phase (silica probably). Superposition of the experimental spectrum with the fitted one, the $R^2 = 0.99$ and $\chi^2<0.01$ attest to the excellent quality of the decomposition. Fe valence state (Table 9) determined in the precipitated smectites using STXM at Fe L-edge (Figure 7) was in accordance with the dioctahedral smectites (i.e. montmorillonite and nontronite).

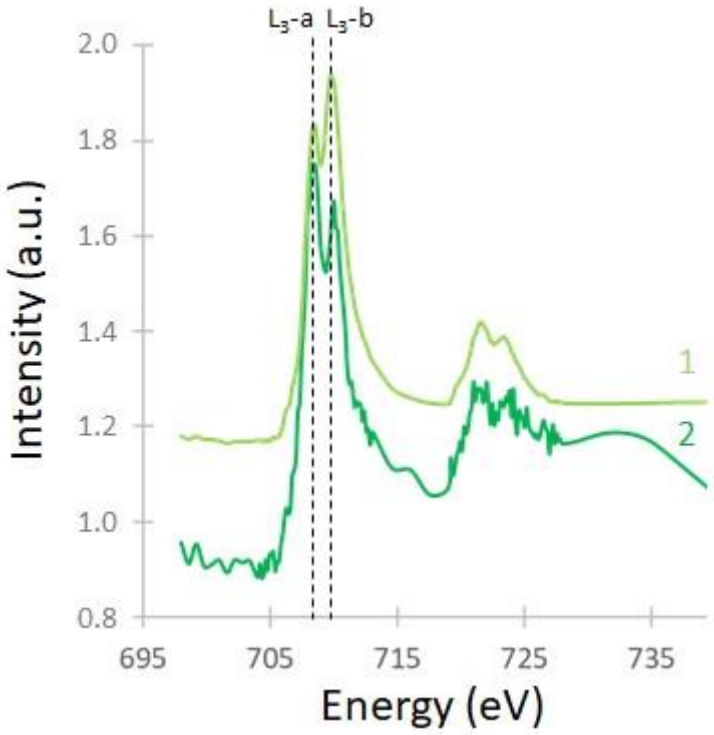

Figure 7: STXM Fe L-edge spectra obtained in the Si-Fe-O and/or Si-Mg-O phases (identified as smectites by STXM at Si K-edge and HRTEM, Figure 4 and Figure 6 respectively) along the gel surface in the CBG-containing system suggesting mixed iron valence in reported in Table 9.

Table 9: Decomposition of the Si K-edge spectra (in green, Figure 4-d) and Fe L-edge (Figure 7) obtained in the phyllosilicates, along the gel surface at the AVM glass/steel interface, with CBG in system.

Edge	decomposition (±2)	R^2	χ^2
Si K	54% SWy2 montmorillonite + 17% NAu2 nontronite + 26% $SiO_{2(am)}$	0.99	0.004
Fe L, spectrum 1	32% Fe^{II} + 68% Fe^{III}	0.98	0.02
Fe L, spectrum 2	53% Fe^{II} + 47% Fe^{III}	0.94	0.01

After one-year of reaction, AVM glass formed a 5 µm-thick Na-depleted GALs in both systems (with and without CBG). We noticed that the concentration of Si in PG and gel were unchanged, and that no Fe precipitated in the gels. This result is also supported by the absence of secondary phases on the top of the gels. Therefore, it is possible to conclude that the gel formed in the two systems resulted from interdiffusion along with B dissolution, although no direct observations for B have been supplied. Pores

of 14 to 20 nm in diameter were detected, revealing an unclogged porosity. Neither the CBG addition, nor the increase in pH have had a significant impact on glass alteration in the tested conditions. Rates calculated from gel thickness are in average 32 times smaller than the initial dissolution rate at the same pH, temperature and solution composition conditions. The absence of any CBG effect on AVM glass durability is confirmed at various time points, according to the gel thickness measured over time through identical mockups run for 6 and 24 months (Figure 8). Indeed, the quantities of altered glass follow the same trend, and the alteration rate drop is close with and without CBG, reaching $r_0^{Cox,\ 70°C}/53$ after 24 months. Hence the rate drop was probably caused by a reduced diffusion of species through the gel layer, even if it is not excluded that both passivation effects and chemical affinity coexist (the first one being predominant). Indeed many studies highlight that the only affinity-limited glass dissolution is not enough to explain the context-dependant rate drop [80]–[82], and a residual rate could be obtained mainly with the amorphous layer [83].

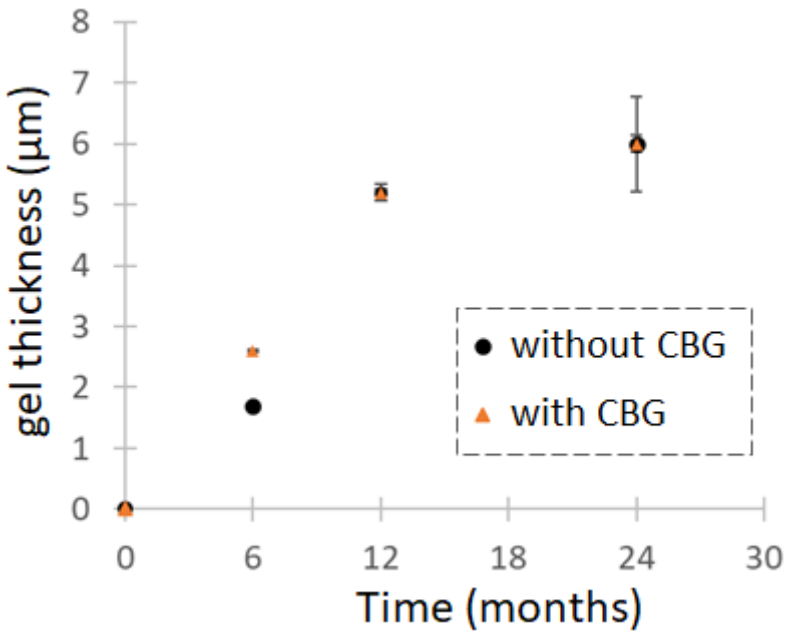

Figure 8: gel thicknesses measured on the AVM glass/C-steel/claystone mockups altered for 6, 12 and 24 months without (black points) and with CBG (orange triangles). The error bars (standard deviations) are indicated for each value but are sometimes hidden by the measurement point.

4) Conclusions

The chemical durability of AVM V4 non-radioactive glass was evaluated through two experimental mockups including C-steel, Callovo-Oxfordian (Cox) claystone and either the presence or absence of a cementitious bentonite grout (CBG). Solid-state characterizations were performed at the glass/C-steel interface for both CBG-free and CBG-containing systems. This study investigates on the coupled processes of steel corrosion and glass alteration, focusing on the influence of corrosion products on the formation and passivating properties of the glass alteration layer.

No Fe/Mg silicate mineral resulting from glass alteration and C-steel corrosion were formed. The presence of CBG did not hinder the formation of the amorphous gel layer on AVM glass surface. This result is notable, as ordered Fe-rich silicate networks, observed in other nuclear glasses such as SON68,

can negatively affect the properties of the alteration layer in presence of an iron source. Under the tested conditions, CBG had no direct impact on glass alteration. The gel maintained an open porosity, with pore sizes ranging from 14 to 20 nm. Glass alteration rates were primarily governed by reduced diffusion through the gel layer and the chemical affinity related to silica concentrations in solution. The moderate alkalinity induced by CBG (pH 8-10 at 70°C) did not affect glass dissolution but was sufficient to ensure the stability of magnetite, which formed an interfacial iron oxide a few hundred nanometers thick. This magnetite layer may contribute to reducing the corrosion rate of C-steel under repository conditions by acting as a diffusion barrier that controls iron release. These findings are critical for refining predictions of multi-barrier system behavior and improving model extrapolation at the waste package scale.

Contribution list

C.C. contributed at all of the experimental characterizations and wrote the paper with A.D., S.G. and P.D.. D.N., A.D., P.D. and C.C. realized the thermodynamic diagram. Results were analyzed and interpreted by C.C., D.N., S.G., and P.D.. The thin foils prepared by FIB and TEM characterizations were performed respectively by E.G., and I.M.. The STXM analyses were conducted by C.C., A.D., E.F., D.N., J.J.D., and P.D.. The experiment was designed and set up by C.M., F.T., S.G., N. M., D.N., and P.D.. All the authors reviewed the paper and approved its final version.

Aknowledgement and funding statement

The authors gratefully acknowledge the French Alternative Energies and Atomic Energy Commission (CEA), the French National Centre for Scientific Research (CNRS) and French National Radioactive Waste Management Agency (Andra), for their financial support. The authors are also thankful to the Canadian Light source (CLS, Canada) and the Optimized Light Source of Intermediate Energy to LURE (SOLEIL, France) for synchrotron beam time allocation. CLS is supported by the Canada Foundation for Innovation (CFI), the National Sciences and Engineering Research Council (NSERC), the National Research Council (NRC), the Canadian Institutes of Health Research (CIHR), the Government of Saskatchewan and the University of Saskatchewan. The CIMAP laboratory thanks to the French state managed by the National Research Agency through the “Investissements d’Avenir” program which reference is “ANR-11-EQPX-0020”, by the Normandie Region and the “Fonds Européen de Développement Régional” FEDER.

References

[1] ANDRA, “Dossier 2005 Argile: synthesis – evaluation of the feasibility of a geological repository in an argillaceous formation, collection les rapports,” ANDRA (agence nationale pour la gestion des déchets radioactifs), Chatenay- Malabry, France, 2005.

[2] J. Bonnet *et al.*, “Chemical and Mineralogical Characterizations of a Low-Ph Cementitious Material Designed for the Disposal Cell of the High-Level Radioactive Waste (HLW),” *SSRN Electron. J.*, vol. 162, no. September, p. 107013, 2022, doi: 10.2139/ssrn.4024185.

[3] M. Robineau, R. Sabot, M. Jeannin, V. Deydier, D. Crusset, and P. Refait, “Mechanisms of localized corrosion of carbon steel associated with magnetite/mackinawite layers in a cement grout,” *Mater. Corros.*, vol. 72, no. 1–2, pp. 194–210, 2021.

[4] H. Verron *et al.*, “Experimental study of pyrite oxidation at 100 °c: implications for deep geological radwaste repository in claystone,” *Minerals*, vol. 9, no. 7, pp. 1–16, 2019, doi: 10.3390/min9070427.

[5] P. Frugier, T. Chave, S. Gin, and J. E. Lartigue, “Application of the GRAAL model to leaching experiments with SON68 nuclear glass in initially pure water,” *J. Nucl. Mater.*, vol. 392, no. 3, pp. 552–567, 2009, doi: 10.1016/j.jnucmat.2009.04.024.

[6] P. Jollivet, F. Angeli, C. Cailleteau, F. Devreux, P. Frugier, and S. Gin, “Investigation of gel porosity clogging during glass leaching,” *J. Non. Cryst. Solids*, vol. 354, no. 45, pp. 4952–4958, 2008, doi: http://dx.doi.org/10.1016/j.jnoncrysol.2008.07.023.

[7] D. Rébiscoul, F. Rieutord, F. Né, P. Frugier, R. Cubitt, and S. Gin, “Water penetration mechanisms in nuclear glasses by X-ray and neutron reflectometry,” *J. Non. Cryst. Solids*, vol. 353, no. 22–23, pp. 2221–2230, 2007, doi: 10.1016/j.jnoncrysol.2007.03.002.

[8] É. Y. Vernaz, S. Gin, C. Jegou, and I. Ribet, “Present understanding of R7T7 glass alteration kinetics and their impact on long-term behavior modeling,” *J. Nucl. Mater.*, vol. 298, pp. 27–36, 2001.

[9] E. Y. Vernaz and J. L. Dussossoy, “Current state of knowledge of nuclear waste glass corrosion mechanisms: the case of R7T7 glass,” *Appl. Geochemistry*, vol. 7, pp. 13–22, 1992.

[10] G. S. Frankel *et al.*, “Recent Advances in Corrosion Science Applicable To Disposal of High-Level Nuclear Waste,” *Chem. Rev.*, vol. 121, no. 20, pp. 12327–12383, Oct. 2021, doi: 10.1021/acs.chemrev.0c00990.

[11] S. Gin, J.-M. Delaye, F. Angeli, and S. Schuller, “Aqueous alteration of silicate glass: state of knowledge and perspectives,” *npj Mater. Degrad.*, vol. 5, no. 1, p. 42, 2021, doi: 10.1038/s41529-021-00190-5.

[12] N. Valle, A. Verney-Carron, J. Sterpenich, G. Libourel, E. Deloule, and P. Jollivet, “Elemental and isotopic (29Si and 18O) tracing of glass alteration mechanisms,” *Geochim. Cosmochim. Acta*, vol. 74, pp. 3412–3431, 2010.

[13] S. Gin *et al.*, “Dynamics of self-reorganization explains passivation of silicate glasses,” *Nat. Commun.*, vol. 9, no. 1, p. 2169, 2018.

[14] D. Ngo *et al.*, “Spectroscopic ellipsometry study of thickness and porosity of the alteration layer formed on international simple glass surface in aqueous corrosion conditions,” *npj Mater. Degrad.*, vol. 2, no. 1, pp. 1–9, 2018.

[15] S. Gin *et al.*, “A General Mechanism for Gel Layer Formation on Borosilicate Glass under Aqueous Corrosion,” *J. Phys. Chem. C*, 2020.

[16] R. Hellmann *et al.*, “Nanometre-scale evidence for interfacial dissolution-reprecipitation control of silicate glass corrosion,” *Nat. Mater.*, vol. 14, no. 3, pp. 307–311, 2015, doi: 10.1038/nmat4172.

[17] S. Gin *et al.*, “The fate of silicon during glass corrosion under alkaline conditions: a mechanistic and kinetic study with the international simple glass,” *Geochim. Cosmochim. Acta*, vol. 151, pp. 68–85, 2015.

[18] K. Damodaran, S. Gin, J.-V. De Montgolfier, C. Jegou, and J.-M. Delaye, “Behavior of B in passivating gels formed on International Simple Glass in acid and basic pH,” *J. Non. Cryst. Solids*, vol. 598, p. 121938, 2022.

[19] P. Frugier *et al.*, “SON68 nuclear glass dissolution kinetics: Current state of knowledge and basis of the new GRAAL model,” *J. Nucl. Mater.*, vol. 380, no. 1, pp. 8–21, 2008, doi: http://dx.doi.org/10.1016/j.jnucmat.2008.06.044.

[20] B. M. J. Thien, N. Godon, A. Ballestero, S. Gin, and A. Ayral, “The dual effect of Mg on the long-term alteration rate of AVM nuclear waste glasses,” *J. Nucl. Mater.*, vol. 427, no. 1–3, pp. 297–310, 2012.

[21] H. Aréna *et al.*, “Impact of Fe, Mg and Ca elements on glass alteration: Interconnected processes,” *Geochim. Cosmochim. Acta*, vol. 239, pp. 420–445, 2018, doi: 10.1016/j.gca.2018.08.007.

[22] X. Guo, S. Gin, and G. S. Frankel, “Review of corrosion interactions between different materials relevant to disposal of high-level nuclear waste,” *npj Mater. Degrad.*, vol. 4, no. 1, p. 34, 2020, doi: 10.1038/s41529-020-00140-7.

[23] H. Aréna *et al.*, “Impact of Zn, Mg, Ni and Co elements on glass alteration: Additive effects,” *J. Nucl. Mater.*, vol. 470, pp. 55–67, 2016, doi: 10.1016/j.jnucmat.2015.11.050.

[24] P. Jollivet *et al.*, “Effect of clayey groundwater on the dissolution rate of the simulated nuclear waste glass SON68,” *J. Nucl. Mater.*, vol. 420, no. 1–3, pp. 508–518, 2012.

[25] C. Carriere *et al.*, “Influence of iron corrosion on nuclear glass alteration processes: nanoscale investigations of the iron-bearing phases,” *Corros. Eng. Sci. Technol.*, vol. 52, 2017, doi: 10.1080/1478422X.2017.1306962.

[26] C. Carrière *et al.*, “Use of nanoprobes to identify iron-silicates in a glass/iron/argillite system in deep geological disposal,” *Corros. Sci.*, p. 108104, Jul. 2019, doi: 10.1016/j.corsci.2019.108104.

[27] C. Carriere *et al.*, “The fate of Si and Fe while nuclear glass alters with steel and clay,” *npj Mater. Degrad.*, vol. 5, no. 1, 2021, doi: 10.1038/s41529-021-00160-x.

[28] C. Carrière *et al.*, “New insights of Auger spectroscopy for the identification of Fe-Si compounds in iron/glass corrosion systems at nanoscale,” *J. Electron Spectros. Relat. Phenomena*, vol. 235, pp. 51–59, Aug. 2019, doi: 10.1016/j.elspec.2019.07.005.

[29] E. Burger, D. Rebiscoul, F. Bruguier, M. Jublot, J. E. Lartigue, and S. Gin, “Impact of iron on nuclear glass alteration in geological repository conditions: A multiscale approach,” *Appl. Geochemistry*, vol. 31, pp. 159–170, 2013, doi: 10.1016/j.apgeochem.2012.12.016.

[30] G. De Combarieu *et al.*, “Glass–iron–clay interactions in a radioactive waste geological disposal: an integrated laboratory-scale experiment,” *Appl. Geochemistry*, vol. 26, no. 1, pp. 65–79, 2011.

[31] M. L. Schlegel *et al.*, “Alteration of nuclear glass in contact with iron and claystone at 90° C

under anoxic conditions: Characterization of the alteration products after two years of interaction," *Appl. geochemistry*, vol. 70, pp. 27–42, 2016.

[32] R. Bouakkaz, A. Abdelouas, Y. El Mendili, K. David, and B. Grambow, "Alteration of 29Si-doped SON68 borosilicate nuclear waste glass in the presence of near field materials," *Appl. Geochemistry*, vol. 111, no. September, p. 104436, 2019, doi: 10.1016/j.apgeochem.2019.104436.

[33] H. Aréna *et al.*, "Impact of iron and magnesium on glass alteration: Characterization of the secondary phases and determination of their solubility constants," *Appl. Geochemistry*, vol. 82, pp. 119–133, 2017, doi: 10.1016/j.apgeochem.2017.04.010.

[34] C. Mohanty, X. Guo, H. Kaya, S. Gin, S. H. Kim, and J. Lian, "Long-term interactive corrosion between International Simple Glass and stainless steel," *npj Mater. Degrad. Degrad.*, vol. 66, no. 50, pp. 1–15, 2022, doi: 10.1038/s41529-022-00262-0.

[35] G. L. McVay and C. Q. Buckwalter, "Effect of Iron on Waste-Glass Leaching," *J. Am. Ceram. Soc.*, vol. 66, pp. 170–177, 1983.

[36] C. Carrière *et al.*, "AVM nuclear glass/steel/claystone system altered by Callovo–Oxfordian poral water with and without cement–bentonite grout at 70°C," *Mater. Corros.*, no. April, 2020, doi: 10.1002/maco.202011766.

[37] L. Sessegolo *et al.*, "Nuclear waste glass alteration under the influence of iron, claystone, and cementitious grout: an integral study," *J. Nucl. Mater.*, p. 155253, 2024.

[38] P. Frugier, C. Martin, I. Ribet, T. Advocat, and S. Gin, "The effect of composition on the leaching of three nuclear waste glasses: R7T7, AVM and VRZ," *J. Nucl. Mater.*, vol. 346, no. 2, pp. 194–207, 2005.

[39] S. Narayanasamy, "Influence of composition on vapor hydration of AVM nuclear glasses." Ecole nationale supérieure Mines-Télécom Atlantique Bretagne Pays de la Loire, 2019.

[40] N. Donzel, S. Gin, F. Augereau, and M. Ramonda, "Study of gel development during SON68 glass alteration using atomic force microscopy. Comparison with two simplified glasses," *J. Nucl. Mater.*, vol. 317, no. 1, pp. 83–92, 2003, doi: https://doi.org/10.1016/S0022-3115(02)01705-1.

[41] P. Dillmann, S. Gin, D. Neff, L. Gentaz, and D. Rebiscoul, "Effect of natural and synthetic iron corrosion products on silicate glass alteration processes," *Geochim. Cosmochim. Acta*, vol. 172, pp. 287–305, 2016, doi: 10.1016/j.gca.2015.09.033.

[42] F. A. Martin, C. Bataillon, and M. L. Schlegel, "Corrosion of iron and low alloyed steel within a water saturated brick of clay under anaerobic deep geological disposal conditions: An integrated experiment," *J. Nucl. Mater.*, vol. 379, no. 1, pp. 80–90, 2008, doi: http://dx.doi.org/10.1016/j.jnucmat.2008.06.021.

[43] C. Bataillon *et al.*, "Corrosion modelling of iron based alloy in nuclear waste repository," *Electrochim. Acta*, vol. 55, no. 15, pp. 4451–4467, 2010.

[44] D. Crusset *et al.*, "Corrosion of carbon steel components in the French high-level waste programme: evolution of disposal concept and selection of materials," *Corros. Eng. Sci. Technol.*, vol. 52, no. sup1, pp. 17–24, 2017.

[45] A. Michelin, E. Drouet, E. Foy, J. J. Dynes, D. Neff, and P. Dillmann, "Investigation at the nanometre scale on the corrosion mechanisms of archaeological ferrous artefacts by STXM," *J. Anal. At. Spectrom.*, vol. 28, no. 1, pp. 59–66, 2013.

[46] Y. Leon, P. Dillmann, D. Neff, M. L. Schlegel, E. Foy, and J. J. Dynes, “Interfacial layers at a nanometre scale on iron corroded in carbonated anoxic environments,” *RSC Adv.*, vol. 7, no. 33, pp. 20101–20115, 2017, doi: 10.1039/C7RA01600J.

[47] M. L. Schlegel, C. Bataillon, K. Benhamida, C. Blanc, D. Menut, and J.-L. Lacour, “Metal corrosion and argillite transformation at the water-saturated,” *Appl. Geochem.*, vol. 23, pp. 2619– 2633, 2008.

[48] Y. Leon *et al.*, “Interfacial layer on archaeological mild steel corroded in carbonated anoxic environments studied with coupled micro and nano probes,” *Corros. Sci.*, vol. 88, pp. 23–35, 2014, doi: 10.1016/j.corsci.2014.07.005.

[49] J. Han, D. Young, S. Nešić, and A. Tripathi, “Chemistry and Structure of the Passive Film on Mild Steel in CO2 Corrosion Environments,” *Ind. Eng. Chem. Res.*, vol. 48, pp. 6296–6302, 2009.

[50] D. Rebiscoul *et al.*, “Morphological evolution of alteration layers formed during nuclear glass alteration: new evidence of a gel as a diffusive barrier,” *J. Nucl. Mater.*, vol. 326, no. 1, pp. 9–18, 2004.

[51] C. Cailleteau *et al.*, “Insight into silicate-glass corrosion mechanisms,” *Nat. Mater.*, vol. 7, no. 12, p. 978, 2008.

[52] N. Michau and X. Bourbon, “French Patent 3031 103. Coulis cimentaire pour remplissage d’un espace annulaire autour d’une alvéole de stockage de déchets radioactifs creusée dans un milieu argileux,” 2014.

[53] E. C. Gaucher *et al.*, “A robust model for pore-water chemistry of clayrock,” *Geochim. Cosmochim. Acta*, vol. 73, no. 21, pp. 6470–6487, 2009, doi: http://dx.doi.org/10.1016/j.gca.2009.07.021.

[54] S. Rajsiri, B. W. Kempshall, S. M. Schwarz, and L. A. Giannuzzi, “FIB damage in silicon: amorphization or redeposition?,” *Microsc. Soc. Am.*, 2002.

[55] L. A. Giannuzzi, R. Geurts, and J. Ringnalda, “2 keV Ga+ FIB Milling for Reducing Amorphous Damage in Silicon,” *Microsc. Microanal.*, vol. 11, no. S02, 2005, doi: 10.1017/s1431927605507797.

[56] F. Bourdelle, T. Parra, O. Beyssac, C. Chopin, and F. Moreau, “Ultrathin section preparation of phyllosilicates by Focused Ion Beam milling for quantitative analysis by TEM-EDX,” *Appl. Clay Sci.*, vol. 59–60, pp. 121–130, 2012, doi: 10.1016/j.clay.2012.02.010.

[57] K. V Kaznatcheev, C. Karunakaran, U. D. Lanke, S. G. Urquhart, M. Obst, and A. P. Hitchcock, “Soft X-ray spectromicroscopy beamline at the CLS: Commissioning results,” *Nucl. Instruments Methods Phys. Res. Sect. A Accel. Spectrometers, Detect. Assoc. Equip.*, vol. 582, no. 1, pp. 96–99, 2007.

[58] R. Belkhou *et al.*, “HERMES: A soft X-ray beamline dedicated to X-ray microscopy,” *J. Synchrotron Radiat.*, vol. 22, pp. 968–979, 2015, doi: 10.1107/S1600577515007778.

[59] F. Bourdelle *et al.*, “Quantification of the ferric/ferrous iron ratio in silicates by scanning transmission X-ray microscopy at the Fe L2,3 edges,” *Contrib. to Mineral. Petrol.*, vol. 166, no. 2, pp. 423–434, 2013, doi: 10.1007/s00410-013-0883-4.

[60] J. J. Dynes *et al.*, “Speciation and Quantitative Mapping of Metal Species in Microbial Biofilms Using Scanning Transmission X-ray Microscopy,” *Environ. Sci. Technol.*, vol. 40, no. 5, pp. 1556–1565, 2006, doi: 10.1021/es0513638.

[61] D. Cabaret *et al.*, “Medium range structure of borosilicate glasses from Si K-edge XANES: A combined approach based on multiple scattering and molecular dynamics calculations,” *J. Non. Cryst. Solids*, vol. 289, no. 1–3, pp. 1–8, 2001, doi: 10.1016/S0022-3093(01)00733-5.

[62] C. Levelut, D. Cabaret, M. Benoit, P. Jund, and A.-M. Flank, “Multiple scattering calculations of the XANES Si K-edge in amorphous silica,” *J. Non. Cryst. Solids*, vol. 293, pp. 100–104, 2001.

[63] D. de Ligny *et al.*, “Silica polymorphs, glass and melt: An in situ high temperature XAS study at the Si K-edge,” *J. Non. Cryst. Solids*, vol. 355, no. 18–21, pp. 1099–1102, 2009, doi: 10.1016/j.jnoncrysol.2008.11.038.

[64] E. Giffaut *et al.*, “Andra thermodynamic database for performance assessment: ThermoChimie,” *Appl. Geochemistry*, vol. 49, pp. 225–236, 2014, doi: https://doi.org/10.1016/j.apgeochem.2014.05.007.

[65] H. Gailhanou *et al.*, “Effects of a thermal perturbation on mineralogy and pore water composition in a clay-rock: An experimental and modeling study,” *Geochim. Cosmochim. Acta*, vol. 197, pp. 193–214, 2017, doi: 10.1016/j.gca.2016.10.004.

[66] M. Robineau *et al.*, “Galvanic corrosion of carbon steel in anoxic conditions at 80° C associated with a heterogeneous magnetite (Fe3O4)/mackinawite (FeS) layer,” *Electrochim. Acta*, vol. 255, pp. 274–285, 2017.

[67] J. Goethals *et al.*, “Interaction between carbon steel and low-pH bentonitic cement grout in anoxic, high temperature (80 °C) and spatially heterogeneous conditions,” *Corros. Sci.*, vol. 211, no. November 2022, p. 110852, 2023, doi: 10.1016/j.corsci.2022.110852.

[68] I. Azoulay, C. Rémazeilles, and P. Refait, “Determination of standard Gibbs free energy of formation of chukanovite and Pourbaix diagrams of iron in carbonated media,” *Corros. Sci.*, vol. 58, pp. 229–236, 2012, doi: http://dx.doi.org/10.1016/j.corsci.2012.01.033.

[69] C. Bataillon, F. Bouchon, C. Chainais-Hillairet, J. Fuhrmann, E. Hoarau, and R. Touzani, “Numerical methods for the simulation of a corrosion model with moving oxide layer,” *J. Comput. Phys.*, vol. 231, no. 18, pp. 6213–6231, Jul. 2012, doi: 10.1016/J.JCP.2012.06.005.

[70] M. L. Schlegel *et al.*, “Corrosion at the carbon steel-clay compact interface at 90°C: Insight into short- and long-term corrosion aspects,” *Corros. Sci.*, vol. 152, no. October 2018, pp. 31–44, 2019, doi: 10.1016/j.corsci.2019.01.027.

[71] J. Agullo, C. Bataillon, and N. Michau, “Preliminary electrochemical corrosion monitoring of iron in mixture cement paste–bentonite,” *Corros. Eng. Sci. Technol.*, vol. 52, no. sup1, pp. 155–161, Apr. 2017, doi: 10.1080/1478422X.2017.1305675.

[72] M. Collin *et al.*, “Structure of International Simple Glass and properties of passivating layer formed in circumneutral pH conditions,” *npj Mater. Degrad.*, vol. 2, no. 1, p. 4, 2018, doi: 10.1038/s41529-017-0025-y.

[73] D. Li, G. M. Bancroft, M. E. Fleet, and X. H. Feng, “Silicon K-edge XANES spectra of silicate minerals,” *Phys. Chem. Miner.*, vol. 22, no. 2, pp. 115–122, 1995, doi: 10.1007/bf00202471.

[74] S. Gin *et al.*, “An international initiative on long-term behavior of high-level nuclear waste glass,” *Mater. Today*, vol. 16, no. 6, pp. 243–248, 2013.

[75] J. D. Vienna, J. V Ryan, S. Gin, and Y. Inagaki, “Current understanding and remaining challenges in modeling long-term degradation of borosilicate nuclear waste glasses,” *Int. J. Appl. Glas. Sci.*, vol. 4, no. 4, pp. 283–294, 2013.

[76] L. Girard, M. Arab, and O. Spalla, “Time resolved alteration process of oxide glasses,” *J. Colloid*

Interface Sci., vol. 319, no. 1, pp. 214–225, 2008.

[77] H. G. Changela and J. C. Bridges, “Alteration assemblages in the nakhlites: Variation with depth on Mars,” *Meteorit. Planet. Sci.*, vol. 45, no. 12, pp. 1847–1867, 2010.

[78] D. M. Moore and J. Hower, “Ordered interstratification of dehydrated and hydrated Na-smectite,” *Clays Clay Miner.*, vol. 34, no. 4, pp. 379–384, 1986.

[79] R. Mosser-Ruck *et al.*, “Effects of temperature, pH, and iron/clay and liquid/clay ratios on experimental conversion of dioctahedral smectite to berthierine, chlorite, vermiculite, or saponite,” *Clays Clay Miner.*, vol. 58, no. 2, pp. 280–291, 2010.

[80] J. Neeway, A. Abdelouas, B. Grambow, and S. Schumacher, “Dissolution mechanism of the SON68 reference nuclear waste glass: new data in dynamic system in silica saturation conditions,” *J. Nucl. Mater.*, vol. 415, no. 1, pp. 31–37, 2011.

[81] J. P. Icenhower and C. I. Steefel, “Experimentally determined dissolution kinetics of SON68 glass at 90 C over a silica saturation interval: Evidence against a linear rate law,” *J. Nucl. Mater.*, vol. 439, no. 1, pp. 137–147, 2013.

[82] T. Advocat *et al.*, “Borosilicate nuclear waste glass alteration kinetics: chemical inhibition and affinity control,” *MRS Online Proc. Libr.*, vol. 506, p. 63, 1997.

[83] S. Gin, C. Jégou, P. Frugier, and Y. Minet, “Theoretical consideration on the application of the Aagaard–Helgeson rate law to the dissolution of silicate minerals and glasses,” *Chem. Geol.*, vol. 255, no. 1–2, pp. 14–24, 2008.